



Motion profile optimization of servo press in deep drawing process of SUS 304 stainless steel sheets

Bor-Tsuen Lin^{1,2} · Kuo-Wang Liu¹ · Tse-Chang Li² · Po-Hsien Li¹ · Chun-Chih Kuo^{1,2}

Received: 9 February 2023 / Accepted: 31 May 2023 / Published online: 23 June 2023
© The Author(s), under exclusive licence to Springer-Verlag London Ltd., part of Springer Nature 2023

Abstract

As servo presses were developed, forming modes became more diverse. However, limited by their own capabilities of motion mechanism, servo presses exhibited differences in the inputted and outputted motion curves, which caused result differences between forming analysis and actual forming. In order to change the servo motion curve to be similar to the actual motion curve, thus improving forming performance during finite element analysis. In this study, MATLAB software was used to construct a model of the motion behavior of a direct-drive servo press. The model was used to predict motion curves and compare metal forming times. However, the error between the motion curve of prediction model and the true motion curve is 13.84%. Therefore, the true motion curve was measured to construct a servo motion trend surface. Then, the servo motion trend surface was integrated with the prediction program to optimize the prediction model. Finally, the finite element analysis software DYNAFORM is used to explore the difference between the thinning ratio and forming force of cylindrical cups with the optimized servo motion curve such as the stepping curve, the coining curve, and the pulsating curve. The analysis result shows that between the optimized and actual servo motion curves, the thinning ratio and forming maximum force error are reduced by 4% and 4.11%, respectively.

Keywords Servo stamping technology · Deep drawing forming process · Motion curve · Optimization

1 Introduction

Servo presses use servomotors to control the angle of rotation, and they can be adjusted to make different motion curves on any position of the top tray by using different velocities. Servo presses provide the flexibility of hydraulic presses, such as adjustable punch velocity and precise position control. In addition, they can record the instantaneous pressure and velocity at any position. Servo presses can improve the metal forming process and production efficiency [1–7]. In the field of metal forming, there has been an increasing need for deep drawing processes. Deep drawing processes are complex forming processes and are related

to material mechanical behaviors such as stretching, bending, and compressing [8–22]. Therefore, during the forming process, the servo press must be designed with the optimal motion curve to respond to different stamping processes. Depending on the requirements of the stamping processes, the optimization of the motion curve has a considerable effect on the production efficiency, production type, and production quality of the servo press [23–29].

In the studies of the predictions and optimization of actual motion curves from servo press, Lin and Tso [30] proposed a hybrid-driven servo press using iterative learning control (ILC). The sensitivity Jacobian is introduced as proportional gain control for smoothing motion curve behavior and increasing the error convergence rate. The result shows the proposed method can effectively make punch position root-mean-square (RMS) errors converge to less than 0.2 mm within five iterations. The precision was also improved to less than 50 μm , equivalent to 35–40% of the original level without the ILC. Song et al. [25] proposed a flexible acceleration and deceleration control algorithm for decreasing the required servo drive energy of the servo press. Then, the optimization model of the drawing eccentric motion profile

✉ Chun-Chih Kuo
cck@nkust.edu.tw

¹ Department of Mechatronics Engineering, National Kaohsiung University of Science and Technology (First Campus), Kaohsiung, Taiwan, Republic of China

² Metal Product Development Technology R&D Center, National Kaohsiung University of Science and Technology (First Campus), Kaohsiung, Taiwan, Republic of China

was established to maximize the production rate, taking into account all boundary conditions, including the maximum velocity and acceleration of the ram, the space and time limit of the material feeder, and the torque and thermal limit of servo motor. The result shows the proposed method obtains the optimal motion profile and the maximum production rate and is validated on heavy servo press. Halicioglu et al. [31] proposed a dynamic model derived by the Lagrange approach for a servo press. Using a servo press with a 50-ton capacity and 200-mm travel as an example, the servo drive and speed reducer selection method are proposed. The dynamic model is used for simulation and actual experiments; the result shows the manufacturing accuracy can reach ± 0.025 , which is acceptably good accuracy for a servo press. Halicioglu et al. [29] used a soft motion for Cr-Ni steel sheet forming based on motion simulation and dynamics for comparing motion behavior under various motion speeds. The result shows soft motion can improve forming speeds and forming quality under thicker material. Chen et al. [32] investigated effects between stamping motion curve and extrusion-drawing process of circular cups. The stamping motion curves are analyzed and confirmed as the best ones. Then, the metal forming simulation software DEFORM is used for analyzing and discussing formability, circular cup dimension, circular cup height, circular cup thickness, extrusion force–displacement curve, stress distribution, and strain distribution. The stamping die is designed and manufactured for conducting experiments to compare actual and simulation results. The result shows that conventional crank motion causes less cup height and greater residual stress and strain and requires higher extrusion force. In comparison, using servo motion curves introduces a greater cup height, less residual stress, and strain.

In recent years, the application of servo presses in deep drawing processes has become more essential. When the press lifts and releases the stress of the blank, the servo pulse motion curve can be used to enable liquid lubricant to be sucked into the mold cavity to lubricate it again. Studies have revealed that compared with conventional curves, pulsating curves can improve the formability of the material. However, the motion behavior of the curve is affected by factors such as signal delay, wear and tear, and size tolerance, which cause the inputted curve parameters to not achieve the expected motion behavior. Accurately predicting the true motion curve can reduce the bias of the finite element analysis result caused by the curve error and thereby increase the accuracy and reliability of the finite element analysis. The true motion behavior of the curve often requires actual measurements, which prolong the time required for development and analysis. Such behavior is not considered during the finite element analysis of other researchers' studies.

This study used MATLAB (the MathWorks, Inc., USA) software to create mathematical models, predict the curve,

and calculate the errors caused by the machines. The errors and the ideal motion curve inputted into the machine were combined to obtain the predicted motion curve and improve the efficiency of development and analysis. The DYNIFORM (ETA, Inc., USA) finite element analysis software was used to perform forming analysis and confirm whether the predicted motion curve improved the accuracy of the finite element analysis. DYNIFORM was also used to compare the thinning ratio of the final products and verify the accuracy of the prediction.

2 Die and materials

During the drawing of cylindrical cups, the top and side material of the cylindrical cup had different flow, and the flange was extruded. This resulted in the corners becoming thin, and sometimes the materials shrunk or cracked. This study used a cylindrical cup drawing die to perform drawing using a servo press, and used DYNIFORM to combine the predicted motion curve, analyze the formability, and compare the predicted and actual forming. To comply with practical production requirements, this study used a cylindrical cup part with a diameter of 41 mm and a depth of 20 mm. The structure of the drawing die is illustrated in Fig. 1. The upper die included the upper die base, punch back plate, punch fix plate, punch, blank holder plate, holder back plate, blank holder insert, and guide post. The lower die included the lower die base, cavity plate, cavity insert, and guide bushing. The stamping die's machining accuracy affects the dimension of the product, and the machining error of the stamping die is less than ± 0.02 mm after measuring. First, the blank was secured in the cavity insert. During drawing, the blank holder and the cavity insert held the blank, then the punch squeezed the material into the cavity. After drawing, the cylindrical cup was inside the cavity insert, and it was pushed out from the hollow bottom. The parameters of the die are demonstrated in Table 1. The material used was a SUS304 stainless steel plate with a thickness of 1.2 mm and thickness tolerances of ± 0.01 mm; its components are

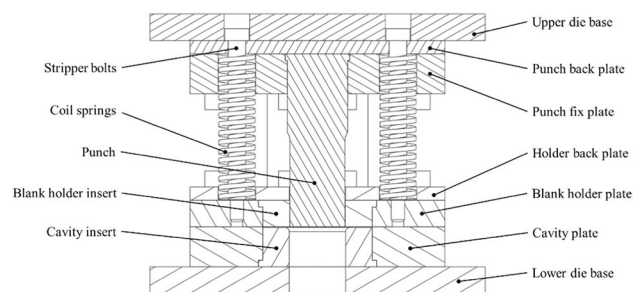


Fig. 1 Structure of the cylindrical cup drawing die

Table 1 Cylindrical cup drawing die measurements

Parameters	Dimensions
Punch (mm)	∅ 41 × 130
Cavity (mm)	∅ 43.4
Cavity radius (mm)	3
Punch radius (mm)	3
Die clearance (mm)	1.2

demonstrated in Table 2. The diameter and tolerance of the blank are 81 mm ± 0.01 mm and machined using WEDM.

3 Kinetic theory model of the direct-drive servo press

3.1 Actuation principles of a direct-drive servo press

Direct-drive servo presses use the servomotor to drive the transmission gear, crankshaft, and linkage mechanism, and produce the stamping action of the slider. Compared with conventional mechanical presses, servo presses can use the servomotor to control rotation direction during mass production and cause the crankshaft to move like a pendulum at the bottom. In comparison, conventional mechanical presses must return to the top dead center before they can execute

the next stamping. Servo presses can effectively reduce the stamping time and improve the production efficiency of the stamping process. The distinguishing characteristic of direct-drive servo presses is their ability to follow the most suitable motion curve according to different products, manufacturing modes, and user requirements. Servo presses can improve problems commonly faced during production, improve the flexibility of the exterior design of products, and increase product diversity.

This study used a 200-ton direct-drive servo press (SEYI SD2 – 200, Shieh Yih Machinery Industry, Taiwan), as shown in Fig. 2a. The maximum stroke velocity was 50 strokes/min. The stamping press’s bottom dead center accuracy affects the accuracy of the forming depth, and the error of bottom dead center is ± 0.01 mm. A schematic of the mechanism is illustrated in Fig. 2b. In the diagram, θ_1 is the angular displacement of the driving crankshaft (rad), θ_2 is the angle of deflection of the follow-up link (rad), r is the length of the crankshaft (mm), and L is the length of the follow-up link (mm). The stroke velocity of the direct-drive servo press was defined as *SPM* (strokes/minute), and the angular velocity of the driving crankshaft (ω , rad/s) was defined as follows:

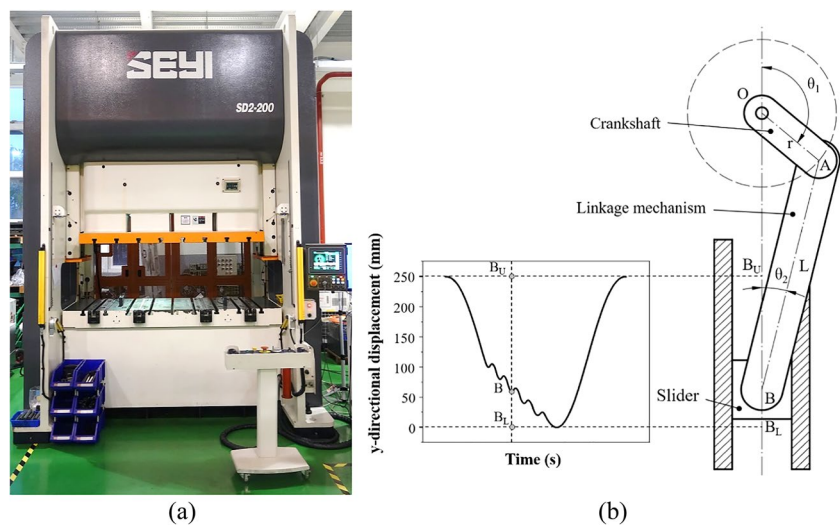
$$\omega = 2\pi \times SPM / 60 \tag{1}$$

To obtain the real-time stroke velocity and the position of the slider of the servo press relative to the bottom dead

Table 2 Components of the SUS304 stainless steel plate

Elements	C	Si	Mn	P	S	Cr	Ni
Minimum-maximum content (wt-%)	≥0.08	≥1.00	≥2.00	≥0.045	≥0.03	18.00-20.00	8.00-10.50
SUS304 (wt-%)	0.042	0.44	0.99	0.034	0.002	18.10	8.010

Fig. 2 a SD2-200 servo press and b schematic of the mechanism of the direct-drive servo press



center (6 o'clock) position during forming, the bottom must be defined as the origin, namely the location of B_L in Fig. 2b. Therefore, the distance $\overline{BB_L}$ is the displacement from the slider to the bottom dead center position. Because $\overline{BB_L} = \overline{OB_L} - \overline{OB}$, the equation reads as follows:

$$\overline{BB_L} = r + L - r \cos \theta_1 - L \sqrt{1 - (r/L)^2 \sin^2 \theta_1} \quad (2)$$

The inputted parameters were changed from the angular displacement of the driving crankshaft to the relationship between the angular velocity and time to obtain the relationship between the angular velocity and the displacement of the slider of the servo press. The calculations are demonstrated in Eq. (3), as follows:

$$\overline{BB_L} = r + L - r \cos(\omega t) - L \sqrt{1 - (r/L)^2 \sin^2(\omega t)} \quad (3)$$

3.2 Theoretical model of the prediction motion curve

This study used MATLAB to construct the theoretical model of the prediction motion curve to obtain the prediction curve of the slider of the servo press with the designated parameters and conditions. Motion curves that are frequently used include the coining curve, the stepping curve, and the pulsating curve.

The prediction program was coded for the aforementioned three types of motion curves.

- Coining curve: The forming parameters include the stroke velocity (strokes/min), bottom dead center coining height (mm), and bottom dead center coining frequency (times). The forming parameters are demonstrated in Fig. 3a.
- Stepping curve: The forming parameters include the stroke velocity (strokes/min), stagnation height (mm), and stagnation time (s). The stepping curve can have multiple stagnations depending on the task. Therefore, each stagnation height and stagnation time must be input. The forming parameters are demonstrated in Fig. 3b.
- Pulsating curve: The forming parameters include the start position of the pulse (mm), lifting velocity (strokes/min), lifting distance (mm), press-in velocity (strokes/min), and press-in distance (mm). The forming parameters are demonstrated in Fig. 3c.

Motor stagnation and punch position during the change of rotation direction were calculated using the forming parameters of the data of each curve. Next, Eq. (2) was used to replace the punch position with the angular position of the servomotor. Finally, the angular displacement

of each stagnation or change of rotation direction was calculated. The following explanation uses the pulsating curve as an example. The forming parameters were as follows: The stroke velocity was 50 strokes/min, the initial pulse height was 20 mm, the lift distance was 0.5 mm, and the press-in distance was 2 mm. The calculations acquired the punch position each time the servomotor changed its rotation direction and obtained the corresponding angular position of the servomotor.

Because the servomotor operated near the peak of the curve, the servomotor changing its rotation direction results in a deceleration effect. Taking the value of the first peak of the pulse as an example, the constant angular acceleration (angular acceleration (α) was constant) was used to calculate the relationship between angular velocity and time. The angular acceleration α was calculated using the rated angular acceleration as the basis. The results revealed that if the angular displacement between two points was too small when the servomotor changed its rotation direction, then the servomotor would prepare to decelerate and rotate in the other direction before it accelerated, and reached the designated stroke velocity to prevent the servomotor from exceeding the required angular displacement during its stroke. Therefore, a conditional program was required to confirm whether the servomotor reached the designated stroke velocity during its stroke. The angular displacement S is the angular displacement required by the servomotor to accelerate to the designated stroke velocity and then decelerate until a standstill. It must be calculated first before the conditional program can be built. The known variables are the angular acceleration α and the designated stroke velocity ω . The angular displacement required for the servomotor to accelerate to the designated angular velocity, as follows:

$$S = \omega^2 / \alpha \quad (4)$$

After the required angular displacement was obtained, the previously established forming parameters were used: the stroke velocity was 50 strokes/min, the initial pulse height was 20 mm, the lift distance was 0.5 mm, and the press-in distance was 2 mm. The forming parameters calculated that the angular displacement S was 0.741 rad. When the punch position reduced from 250 to 20 mm, the angular displacement was 2.603 rad and was greater than the angular displacement of 0.741 rad required for acceleration and deceleration. Therefore, the conditional program entered the first stage of calculations, as demonstrated in Fig. 4. Afterward, the calculations discovered that the relationship between angular velocity and time formed a trapezium, as demonstrated in Fig. 5a. In the figure, $\overline{0a}$ is the acceleration interval, \overline{ab} is the constant velocity interval, and \overline{bc} is the deceleration interval. When the punch position increased from 20 mm to 20.5 mm, the angular displacement

Fig. 3 Three types of motion curves: (a) bottom dead center coining curve, (b) stepping coining curve, and (c) pulsating curve

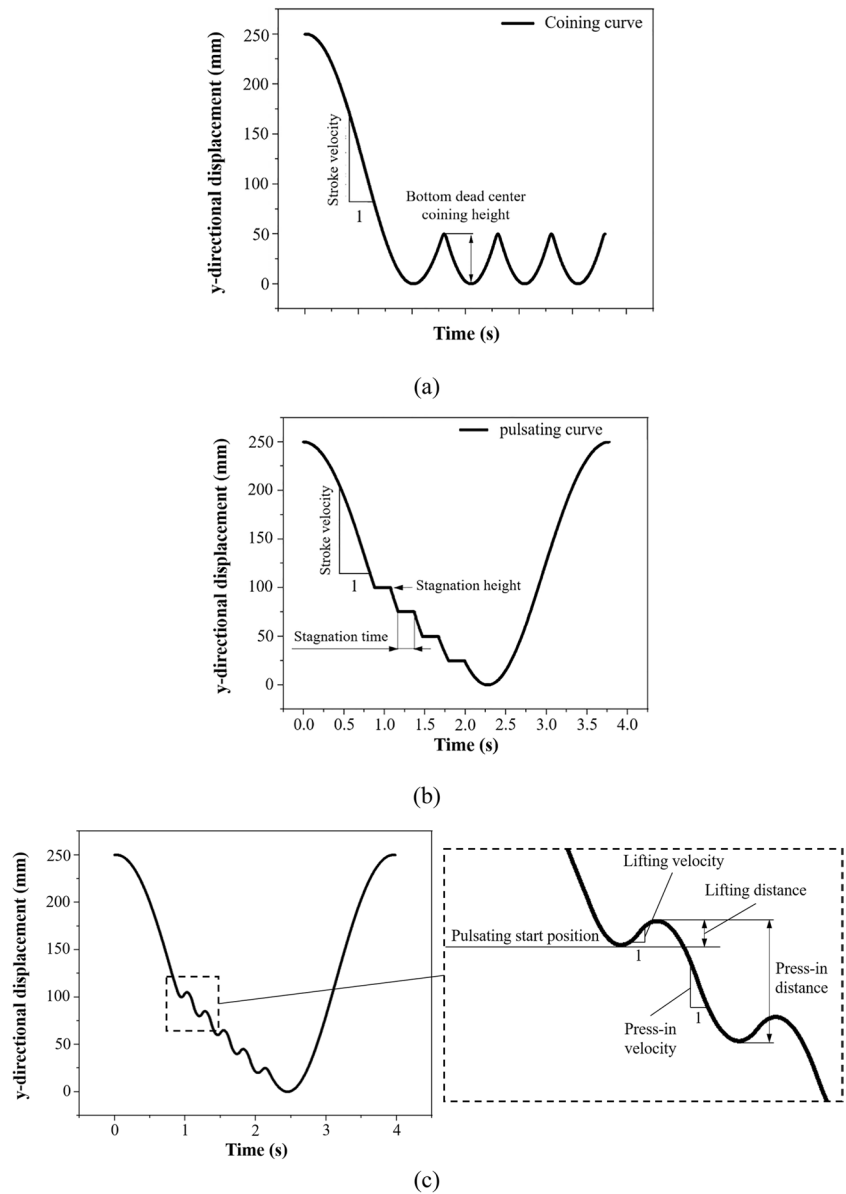


Fig. 4 Program used to determine the angular displacement

```

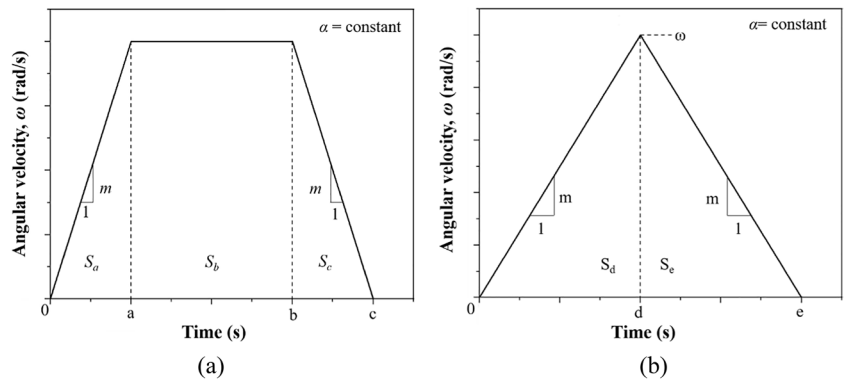
if vib_thi_rad > S_alpha_2
    vib_up_ns = vib_thi_rad - S_alpha_2;
    vib_up_t_1 = linspace(0, sqrt(S_alpha_2/(alpha_2)), vib_seg);
    vib_up_t_mid = linspace(sqrt(S_alpha_2/(alpha_2)), vib_up_ms/v + max(sqrt(S_alpha_2/(alpha_2)), vib_seg), ...);
    vib_up_t2 = linspace(vib_up_ms/v + max(sqrt(S_alpha_2/(alpha_2)), ...), ...);
    sqrt(S_alpha_2/(alpha_2))*2 + vib_up_ms/v, vib_seg);
    vib_up_t = [vib_up_t_1(st,:), vib_up_t_mid(st,:), vib_up_t_2(st,:)];
else
    vib_up_t_1 = linspace(0, sqrt(vib_thi_rad(st,1)/(alpha_2)), vib_seg);
    vib_up_t_2 = linspace(sqrt(vib_thi_rad(st,1)/(alpha_2)), sqrt(vib_thi_rad(st,1)/(alpha_2))*2, vib_seg);
    vib_up_t = [vib_up_t_1(st,:), vib_up_t_2(st,:)];
end
    
```

} First stage
} Second stage

was -0.007 rad and was smaller than the angular displacement of 0.741 rad required for acceleration and deceleration. Therefore, the conditional program entered the second stage of calculations, as demonstrated in Fig. 4. The calculations revealed that the displacement was insufficient; therefore,

the acceleration did not reach the designated stroke velocity. Consequently, the relationship between angular velocity and time formed a triangle, as demonstrated in Fig. 5b. Figure 5b only includes the acceleration interval and the deceleration interval; it does not include the constant velocity interval.

Fig. 5 Relationship between the angular velocity of the servomotor and time: (a) with a constant velocity interval [24] and (b) without a constant velocity interval



The aforementioned calculations demonstrated that two types of relationships were present between angular velocity and time. The first type appeared when the stroke velocity accelerated and reached the designated stroke velocity; the relationship between angular velocity and time had a trapezium shape, as demonstrated in Fig. 5a. The second type appeared when the displacement was insufficient for the stroke velocity to reach the designated stroke velocity; the relationship between angular velocity and time had a triangle shape, as demonstrated in Fig. 5b. The angular displacement is the area under the angular velocity–time curve. The calculations for the two types of angular displacement are as follows:

(a) Trapezium-shaped angular velocity–time curve

$$S_a = S_c = (t \times \omega) / 2 = \omega^2 / 2\alpha \tag{5}$$

$$S_b = S - (S_a + S_c) \tag{6}$$

where $t = \omega/\alpha$, S_a represents the area of the acceleration interval, S_b represents the area of the constant velocity interval, S_c represents the area of the deceleration interval, and S represents the total area. The trapezium-shaped angular velocity–time curve was integrated to obtain the relationship between the angular displacement and time, as demonstrated in Fig. 6a. In the figure, the time interval from 0 to a is the acceleration interval, and it has the form of a quadratic

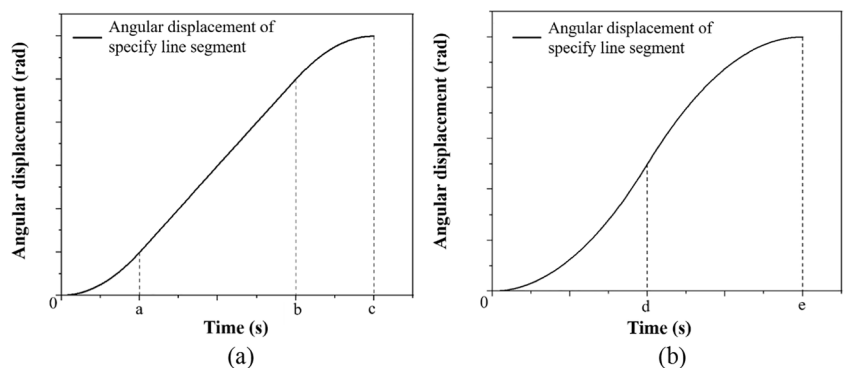
curve that concaves upwards. The time interval from a to b is the constant velocity interval and is a diagonal straight line. Finally, the time interval from b to c is the deceleration interval, and it has the form of a quadratic curve that concaves downwards. During the deceleration interval, the servomotor decelerates and prepares to rotate in the other direction.

(b) Triangular-shaped angular velocity–time curve where $t = \omega/\alpha$, S_d represents the area of the acceleration interval and S_e represents the area of the deceleration interval. The triangular-shaped angular velocity–time curve was integrated to obtain the relationship between angular displacement and time, as demonstrated in Fig. 6b. Figure 6a features a clear acceleration interval, constant velocity interval, and deceleration interval. In comparison, Fig. 6b features an acceleration interval from 0 to d ; however, the angular displacement was insufficient at point d and the angular velocity could not reach the designated angular velocity. Therefore, the deceleration interval from d to e began to decelerate and the servomotor began to prepare to rotate in the other direction during this interval.

$$S_d = S_e = (t \times \omega) / 2 = \omega^2 / 2 \tag{7}$$

The aforementioned equations were used to obtain the position each time the servomotor stagnated or rotated

Fig. 6 Relationship between the angular displacement of the servomotor and time: (a) with a constant velocity interval and (b) without a constant velocity interval



in the other direction. Next, the angular displacement of each point was calculated, and the conditional program demonstrated in Fig. 4 was used to determine whether the displacement was sufficient to enable the servomotor to accelerate to the designated stroke velocity. Afterward, the angular velocity–time curve was integrated to obtain the relationship between angular displacement and the time of each interval. Finally, the relationship between the angular displacement and time of each interval was connected to obtain the complete relationship between angular displacement and time, as demonstrated in Fig. 7. The *x*-axis represents the forming time, and the *y*-axis represents the angular position of the servomotor during forming. The relationship between the angular position of the servomotor and time was used with Eq. (2) to replace the angular position of the servomotor with the punch position and obtain the relationship between the punch position and time. The result was outputted and used to draw the prediction curve, as demonstrated in Fig. 8. The *x*-axis represents the forming time, and the *y*-axis represents the position of the top tray of the servo press during forming.

This study established a theoretical model of the motion behavior of servo presses and designed a program to predict the motion curve. Next, this study compared the prediction curve, expected output motion curve, and true motion curve. The comparison results are demonstrated in Fig. 9. The results revealed that the expected output motion curve did not consider any physical inertia. Therefore, the curve reached the designated stroke velocity from the initial position immediately, and no delay occurred each time the servomotor rotated in the other direction. Therefore, the expected output motion curve exhibited a large time error (Δt_1) as compared with the true motion curve. The prediction curve did not consider the time error caused by factors such as the signal delay of the machine, the machining error of the servo press, the loss of kinetic energy due to friction, or physical

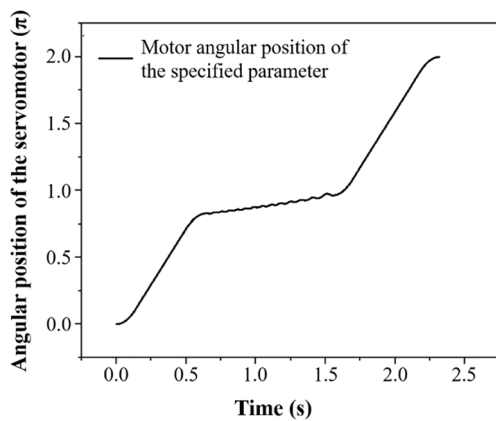


Fig. 7 Relationship between the angular position of the servomotor and time

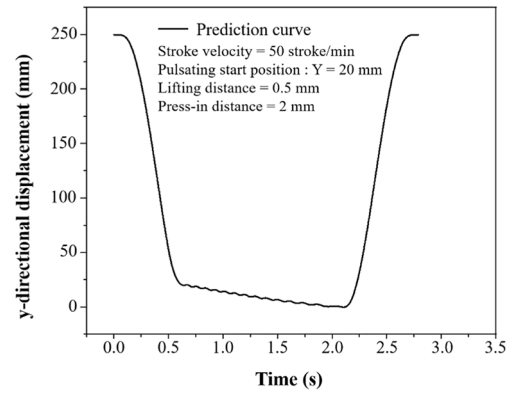


Fig. 8 Prediction curve of the pulsating motion of the slider

inertia. Therefore, when the prediction program calculated the prediction curve, it was unable to estimate the time error (Δt_2) when the servomotor rotated in the other direction.

4 Optimization of the predicted motion curves

The prediction program built for the direct-drive servo press was used to output motion curves. The results revealed that the prediction program did not consider the time error caused by factors such as the signal delay of the machine, the loss of kinetic energy due to friction, or physical inertia. Therefore, the prediction curve and the true motion curve exhibited a time delay. To reduce this time delay and improve the accuracy of the prediction curve, finite element analysis was used to determine the accuracy of the results. The construction of the prediction curve is demonstrated in Fig. 10. The laser measuring system recorded the motion curves generated by executing different pulse steps under pulsating curve forming of the servo press. The pulse intervals of each motion curve were extracted and Origin Pro

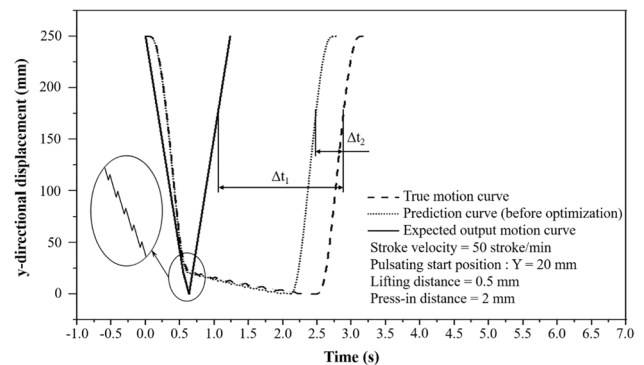


Fig. 9 Comparison of the prediction curve and the true motion curve

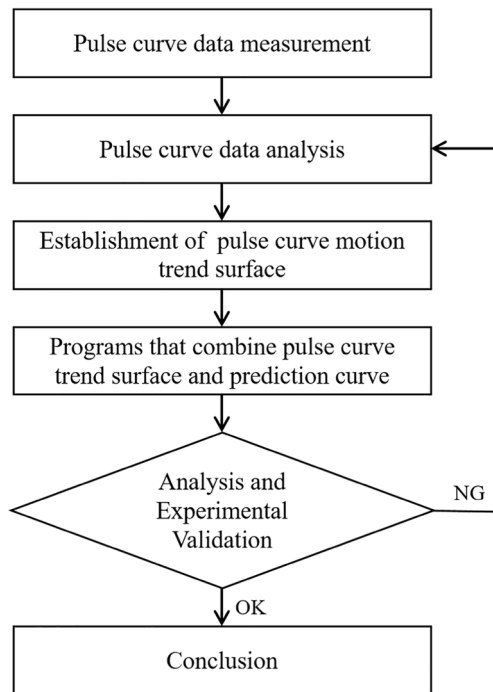


Fig. 10 Construction of the prediction curve

software was used to analyze the motion trend curve of the pulse interval. The motion trend curves with the same pulse steps but with different velocities were combined to create the pulse trend surface, which can predict the motion trajectory using designated pulse steps and any velocity. The pulse trend surface and the prediction program were integrated to complete the prediction program and provide the prediction curve. Finally, DYNAFORM was used to analyze and verify the experimental results.

This study analyzed the motion behavior of servo presses during pulsating curves. When servo presses perform pulsating curves, external factors cause the expected motion behavior to differ from the true motion behavior. During the design and development of new products, the accuracy of formability evaluated by finite element analysis software decreases greatly. To overcome this problem, the motion behavior of the pulsating curve must be measured and analyzed to correct the prediction program and enable the program to accurately predict the true motion behavior, thereby improving the accuracy of the evaluation of formability. The setting of the true motion curve of the servo press was as follows:

- (1) Pulsating motion mode
- (2) Stroke velocity 50 strokes/min
- (3) Pulse start position 20 mm
- (4) Lift distance 0.5 mm
- (5) Press-in distance 2 mm

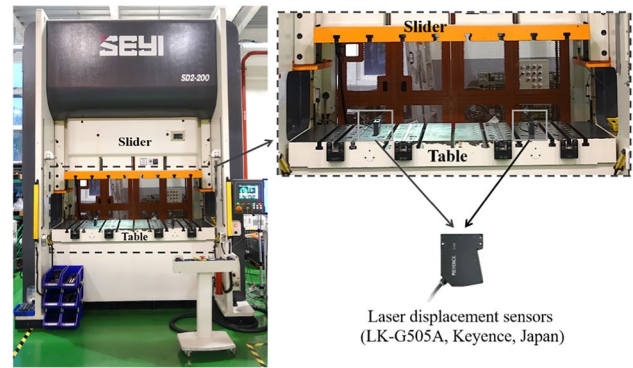


Fig. 11 Installation location of the laser displacement sensor

The laser measuring system was used to measure the motion of the top tray of the servo press. The installation of the laser displacement sensor (LK-G505A, Keyence, Japan) is illustrated in Fig. 11. During data collection, the true outputted signal was collected first. Next, Keyence LK-Navigator software was used to process the data. The measurement parameters were set as follows: Because the surface measured by the laser displacement sensor was neither transparent nor a mirror surface, the measurement mode was set to standard. The filter mode of the measured data output was the moving-average mode, and the frequency of the filter was one sample for every 64 sets of data. The sampling frequency of the measured data was 1000 points/s. After the true motion curve was measured, the point data were input into Origin Pro for postprocessing to enable subsequent construction of the pulse trend surface based on feature data.

This study used the true motion curve measured by the laser measuring system. The point data were inputted into Origin Pro. To identify the motion behavior of the pulsating curve and estimate the time error, feature points were marked on the point data of the true motion curve. The feature points were the position where the pulse of the true motion curve started and finished, as demonstrated in Fig. 12a. Feature point 1 and feature point 2 were positions where the servomotor rotated in the other direction. Therefore, the tangential velocity of these two feature points was 0 mm/s. After the feature points of the true motion curve were marked, feature point 1 was defined as the position where the pulse started and feature point 2 was defined as the position where the pulse finished, so as to independently analyze the pulse behavior of the true motion curve. The pulse interval of the true motion curve was collected, and the results demonstrated that the pulse motion of the top tray of the servo press did not pulse in a diagonal line. Rather, the time required for each pulse became longer as the frequency of pulses increased, causing the pulse interval of the true motion curve to concave slightly upwards. To identify the motion trend curve of the pulse interval

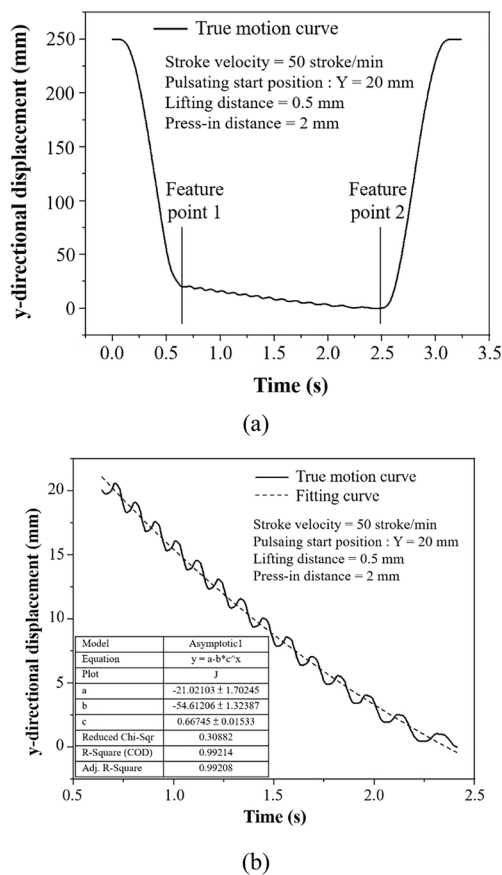


Fig. 12 a Feature points of the true motion curve and (b) fitting curve of the pulse interval of the true motion curve

of the true motion curve, Origin Pro was used for curve fitting. The computational logic used the asymptotic line of exponential functions and the iteration algorithm used the Levenberg–Marquardt method for iterative calculations. The results of the curve fitting are demonstrated in Fig. 12b. The motion trend of the pulse interval of the true motion curve is demonstrated as follows:

$$y = -21.02103 + 54.61206 \times 0.66745^x \tag{15}$$

Adj. R-Square = 0.99208. In the equation, y represents the displacement along the y -axis, and x represents the forming time of the servo press.

To construct the pulse trend surface of the servo press using different pulse steps, different pulse steps were used and the pulsating curves of the servo press functioning under different pulse steps and velocities were collected. The pulse steps used were 1 mm, 3 mm, and 5 mm; the stroke velocities used were multiples of 5 from 5 strokes/min to 50 strokes/min. Afterward, the aforementioned procedures were used to analyze the feature data of the pulsating curve and obtain the pulse trend of the top tray

of the servo press under different pulse steps and stroke velocities. Data were organized according to different pulse steps to obtain the pulse trend surfaces with pulse steps of 1 mm, 3 mm, and 5 mm under different stroke velocities. The pulse trend surfaces with a pulse step of 1 mm, 3 mm, and 5 mm are demonstrated in Fig. 13a, Fig. 13b, and Fig. 13c, respectively. The time represents the time required for forming and the stroke velocity represents the stroke velocity designated for the servo press. The effects of stroke velocity and displacement to time are shown through contour lines and color changes on the pulse trend surface.

For the pulse trend surface with a pulse step of 1 mm, the forming time was the longest when the stroke velocity was 5 strokes/min. If the stroke velocity reached 10 strokes/min, then the forming time required reduced. However, when the stroke velocity increased from 10 to 15 strokes/min, the time reduction was not as evident as the time reduction when the stroke velocity increased from 5 to 10 strokes/min. In fact, the time only decreased marginally. The forming time did not decrease when the stroke velocity increased from 15 strokes/min to 20 strokes/min. The pulse motion trend was highly similar to that of forming time. When the pulse step was 1 mm, the stroke velocity was 15 strokes/min, the maximum stroke velocity. However, if the stroke velocity was increased, factors such as the capability of the servo press and physical inertia limited the motion behavior and the motion behavior could not achieve the expected results. The results of the 3 mm and 5 mm pulse steps were the same as those of the pulse step of 1 mm.

This study performed data analysis using the measured true motion curve and used feature points to extract data. Next, this study used trend analysis to obtain the trend of the pulsating curves when the top tray of the servo press worked under the designated parameters. The pulse trend surface was constructed to predict the motion behavior using different pulse steps and velocities. In addition, to improve the accuracy of the prediction of the program, the pulse trend surface was used in the prediction program. The operation flow of the program was as follows:

- (a) Input the designated parameters of the curve.
- (b) Determine the pulse step of the curve.
- (c) Extract the curve data of the pulse trend surface.
- (d) Calculate and correct the time required to achieve the designated parameters.
- (e) Complete the integration of the pulse trend surface and the prediction program.

First, the parameters required by the pulsating curve were inputted into the program. The parameters inputted were as follows: the stroke velocity was 20 strokes/min, the initial pulse height was 15 mm, the lift distance was

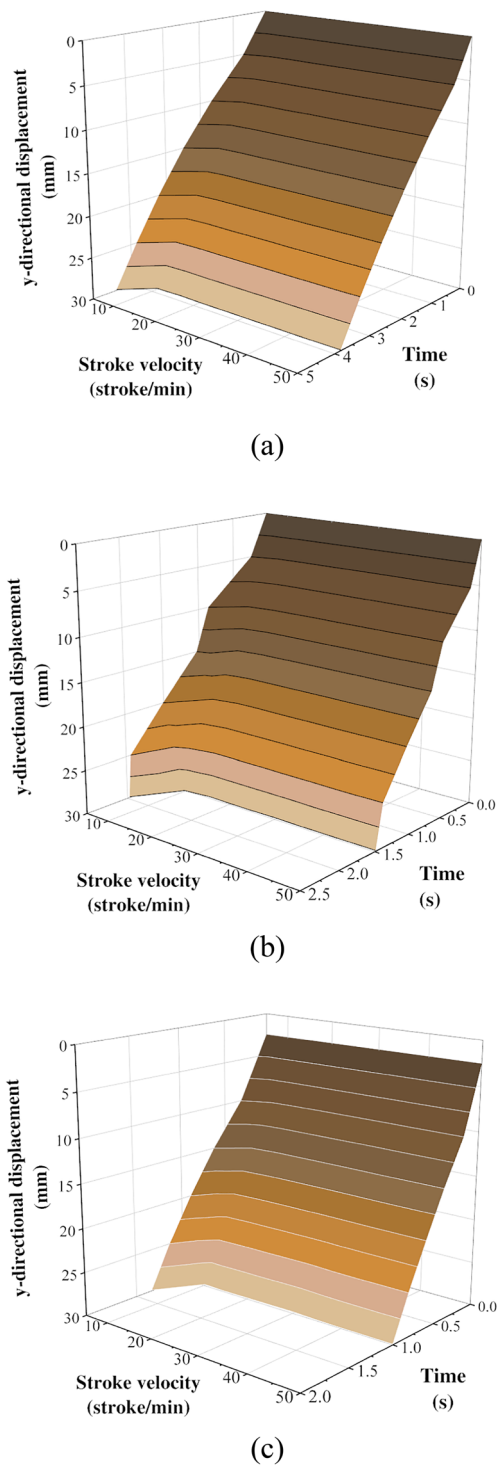


Fig. 13 Changes of the pulse trend surface with different pulse steps: (a) 1 mm, (b) 3 mm, and (c) 5 mm

1 mm, and the press-in distance was 4 mm. The parameters of the pulsating curve have multiple combinations when users predict the pulsating curve. Therefore, the pulse step of the parameters must be calculated first so that the program can select the appropriate pulse trend surface and

predict the motion curve. The pulse step is calculated as follows:

$$\text{press} - \text{in distance} - \text{lift distance} = \text{pulse step}$$

Therefore, if the pulse step is 4 mm – 1 mm = 3 mm, then the pulse trend surface with a pulse step of 3 mm is selected to optimize the predicted motion curve using the aforementioned parameters, as demonstrated in Fig. 13b. After the pulse step is calculated, the curve data of the pulse trend surface is extracted to optimize the prediction program and reduce the time error between the prediction curve and the true motion curve. Because the parameter of the stroke velocity was 20 strokes/min, the pulse trend surface with a pulse step of 3 mm had to be analyzed independently and the pulsating curve with a stroke velocity of 20 strokes/min was extracted from the pulse trend surface for analysis.

After the parameters of the pulsating curve were set, the lift distance and press-in distance were used to calculate the size of the pulse step of the pulsating curve. The pulse step was used to select the pulse trend surface appropriate for the pulsating curve parameters, and the stroke velocity was used to extract the required pulse trend curve. Afterward, the required forming time was calculated using the designated parameters to optimize the prediction program. The process of calculating the required forming time was as follows: First, the parameters of the pulsating curve signified that the position where the pulsating curve performed the pulse motion was $Y = 15$ mm. Therefore, the pulse motion occurred at 15 mm up from the bottom dead center position of the servo press. The total displacement of the pulse motion was 15 mm. After the total displacement of the pulse motion was obtained, the previously extracted pulse trend curve was used to mark the position of –15 mm along the y-axis. The marked position indicated that after the pulse motion, the bottom dead center position moved 15 mm. After the new position was marked, the time required to move between the two positions was calculated to obtain the forming time t , as demonstrated in Fig. 14. The y-axis represented the displacement of the top tray of the servo press after the pulse motion, and the x-axis represented the time required for the pulse motion.

The pulse step was calculated to select the pulse trend surface suitable for the forming parameters. Next, the stroke velocity was used to extract the pulse trend curve required for the optimization of the prediction program from the previously selected pulse trend surface. Finally, the start position of the pulse was used to calculate the time required to initiate and complete the pulse motion. The calculations were used to optimize the prediction program. The optimization adjusted the time. Therefore, the multiplying power of the time adjustment needed to be calculated first. The calculation process was as follows: adjust the magnification equal to t/t_0 , where t represents the forming time before the prediction program was optimized, and t_0 represents the

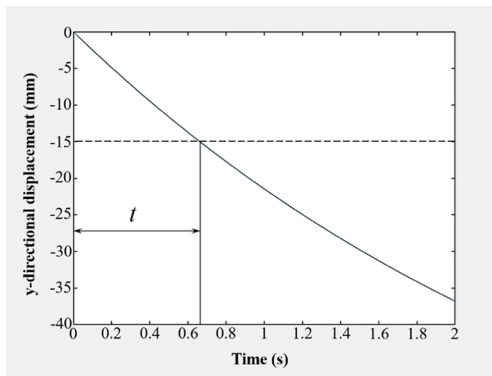


Fig. 14 Time required for the pulse motion under the designated parameters

forming time of the previous stage. The adjustment magnification was input into the prediction program. The program architecture is demonstrated in Fig. 15. During the optimization of the prediction program, the adjustment of the forming time of the pulsating curve was divided into three stages. The first stage split the points of the curve and calculated the time required to travel from one point to the next point. Next, the time differences between each point were placed in a set. The variable vib seg represents the thinning ratio of the curve and was set at 1000; it also represents the number of point data every time the servomotor rotated in the other direction. The second stage used the time difference between each point and used the adjustment multiplying power to adjust the time difference to obtain the optimized time difference. In the third stage, the time differences were adjusted to reduce the time error. Finally, the divided point data were serially connected to complete the optimization of the prediction program and further reduce the time error.

After the prediction program was optimized, its results were compared to confirm its optimization, as demonstrated in Fig. 16. The *x*-axis in Fig. 16 represents the time required for the servo press to perform one pulse motion, and the *y*-axis represents the displacement of the top tray of the servo press during each pulse motion. The results demonstrate that the prediction curve before optimization was

```

vib_t_delta = [ ];
for i = 1:vib_seg-1
    vib_t_delta(i) = vib_t(st,i+1) - vib_t(st,i);
end
vib_t_delta = vib_t_delta*vibration_rate;
vib_t(st,1) = 0;
for i = 1:vib_seg-1
    vib_t(st,i+1) = vib_t(st,i)+vib_t_delta(i);
end
    
```

Fig. 15 Program of the adjustment multiplying power

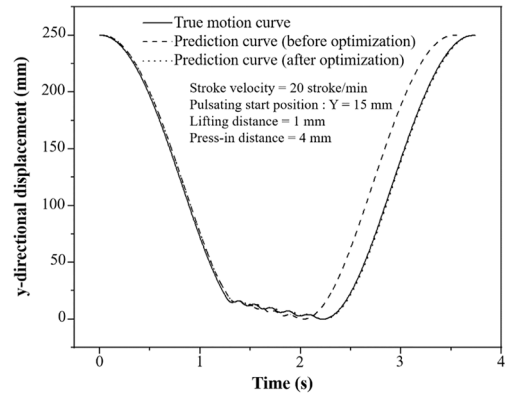


Fig. 16 Comparison of the prediction curves

different from the true motion curve; however, the prediction curve after optimization was similar to the true motion curve and the optimization was effective. Regression analysis was performed to confirm the optimization. The *R*-square before optimization was 0.8412 and the *R*-square after optimization was 0.9051. The *R*-square increased by 0.0639 and demonstrated the optimization of the prediction program.

Finally, the error of the curves before and after optimization was compared. The designated parameters were used and the stroke velocity was adjusted to measure the displacement and time difference of the slider of the servo press. The parameters of each curve were as follows:

- (a) Pulsating curve with a pulse step of 1 mm:

The stroke velocity was 5–50 strokes/min, the start position of the pulse was 15 mm, the lift distance was 1 mm, and the press-in distance was 2 mm.

- (b) Pulsating curve with a pulse step of 3 mm:

The stroke velocity was 5–50 strokes/min, the start position of the pulse was 15 mm, the lift distance was 1 mm, and the press-in distance was 4 mm.

- (iii) Pulsating curve with a pulse step of 5 mm:

The stroke velocity was 5–50 strokes/min, the starting position of the pulse was 15 mm, the lift distance was 1 mm, and the press-in distance was 6 mm.

- (iv) Coining curve:

The stroke velocity was 5–50 strokes/min, the bottom dead center coining height was 5 mm, and the bottom dead center coining frequency was 4 times.

- (e) Stepping curve:

The stroke velocity was 5–50 strokes/min, the inching position was 10 mm, the inching distance was 3 mm, and the stagnation time was 0.1 s.

The measurement methods were as follows: The true motion curve was used as the standard and each 0.1 mm was a node. The time errors between the prediction curve and the true motion curve at each node were calculated, as demonstrated in Fig. 17. Afterward, the absolute values of the time errors were used to avoid positive and negative values canceling each other out and affecting the result. Next, the root mean square error of each motion curve at different times was calculated and the percentage error was recorded. The percentage error was calculated by dividing the root mean square error by the total time required for the whole motion. The errors between the prediction curves and the true motion curve are demonstrated in Table 3. The results demonstrated that when the servo press performed the motion behavior of the pulsating curve, the motion behavior became more unstable as the pulse step increased and the stroke velocity

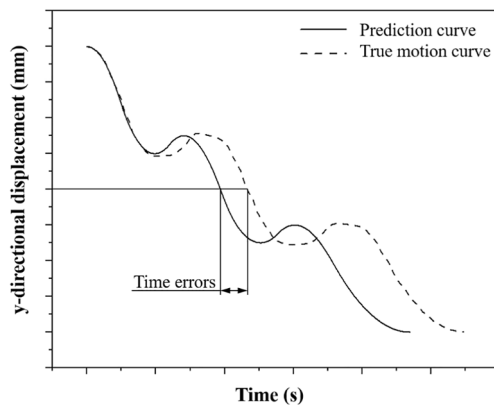


Fig. 17 Schematic of the measurement of the position error

became faster. Consequently, the prediction of the motion behavior became more difficult, and the error of pulsating curves with higher pulse steps was higher compared with the pulsating curve with a pulse step of 1 mm. The largest root mean square error percentage was the pulsating curve with a pulse step of 5 mm (3.16%), followed by the pulsating curve with a pulse step of 3 mm (2.77%) and the pulsating curve with a pulse step of 1 mm (0.81%). The prediction and actual result of the bottom dead center coining curve and the stepping curve are demonstrated in Table 4. The position errors of the stepping curve at different stroke velocities were closer because the servomotor only accelerated and decelerated when the stepping curve was performed, and the servo motor did not change its rotation direction. Therefore, compared to the coining curve, the position error of the stepping curve was smaller. The overall percentage error of the coining curve (2.37%) was smaller than that of the stepping curve (2.67%). The curves were used to calculate the motion trend of the curves and correct the time error of the prediction program. Finally, a prediction curve extremely similar to the true motion curve was produced.

5 Analysis and experimental verification

This study used DYNAFORM software to simulate the servo pulse forming and used the results to compare the forming difference between the predicted and expected output motion curves. The maximum and minimum element size of the punch, blank holder, and cavity was 2 mm and 0.4 mm, and the element size of the blank was $0.1 \times 0.1 \text{ mm}^2$. The punch motion curve was arranged and analyzed using the prediction curve and the expected output motion curve. This study only recorded the drawing process from the moment the punch contacted the material until the punch reached

Table 3 Error between the predicted and true pulsating curves using the SEYI SD2 200-ton servo press

pulse step (mm)	1		3		5		
	Stroke velocity (stroke/min)	mean square error (s)	error percentage (%)	mean square error (s)	error percentage (%)	mean square error (s)	error percentage (%)
5		0.281	0.64	0.327	1.36	0.190	0.95
10		0.358	0.81	0.269	1.12	0.389	1.95
15		0.277	0.63	0.664	2.77	0.378	1.89
20		0.217	0.49	0.398	1.66	0.436	2.18
25		0.239	0.54	0.435	1.81	0.552	2.76
30		0.235	0.53	0.484	2.02	0.604	3.02
35		0.228	0.52	0.514	2.14	0.624	3.12
40		0.231	0.53	0.461	1.92	0.621	3.11
45		0.233	0.53	0.455	1.89	0.622	3.11
50		0.294	0.69	0.510	2.13	0.633	3.16

Table 4 Error between the predicted and true coining curve and stepping curve using the SEYI SD2 200-ton servo press

Curve type	Coining		Stepping	
	mean square error (s)	error percentage (%)	mean square error (s)	error percentage (%)
5	0.128	0.19	0.082	0.51
10	0.441	0.69	0.426	2.67
15	1.020	1.54	0.351	2.19
20	1.190	1.80	0.284	1.78
25	0.793	1.20	0.240	1.50
30	0.586	0.89	0.218	1.36
35	1.031	1.56	0.240	1.50
40	0.974	1.48	0.231	1.45
45	1.271	1.92	0.231	1.45
50	1.563	2.37	0.220	1.38

the bottom dead center position to reduce the time required for DYNAFORM to perform analysis. The analyzed motion curves are demonstrated in Fig. 18. The analysis models were the punch, blank holder, blank, and cavity, as demonstrated in Fig. 19. The coefficient of friction between the SUS304 plate material and the mold cavity was 0.2. During the simulation, isotropic plastic was used to define the deformation of the plate material. The tensile test was used to obtain the engineering stress–strain curve. The tensile test piece conformed to the ASTM E8 standard. The research obtains the load–elongation curve using a universal tensile test machine. The tensile test consists of two stages: In the 1st stage, the test uses a stress control rate of 5 MPa/s before reaching yield stress. In the 2nd stage, the test uses a strain control rate of 15%/min after reaching yield stress to obtain a stress–strain curve for converting into a true stress–strain curve for finite element analysis. Only a load–elongation curve is obtained by conducting a standard tensile stress test. However, some parameters can be obtained by executing some calculations, such as Young’s modulus, yield strength, ultimate tensile strength, and elongations. In order to conduct finite element analysis, the true stress–strain curve is needed. Its true stress–strain curve is demonstrated in Fig. 20. The material parameters used in the analysis software are demonstrated in Table 5.

This study used the experimental and analytical results to compare the thinning ratio and forming force:

(a) Verification of the thinning ratio

The final product used wire electrical discharge machining and an image size measuring instrument to measure the thinning ratio from the center of the final product to the flange. The thinning ratio was measured at every 3 mm

from the center and compared with the analytical value. To obtain more precise measurements and identify the position with the maximum thinning ratio, the servo stepping curve and the bottom dead center coining curve measured the thinning ratio at every 0.5 mm between the interval of 15–33 mm. The pulsating curves measured the thinning ratio at every 0.5 mm between the interval of 15–36 mm. The measured positions of the stepping curve and coining are presented on Fig. 21a. The measured positions of the pulsating curves with a pulse step of 1, 3, and 5 mm are presented on Fig. 21b.

The analytical results of the servo stepping curve are illustrated in Fig. 22a. The figure reveals that the trends of the experiment and analyzed thinning ratios were consistent. The maximum thinning ratio of the experiment was 17.28%, and the maximum thinning ratio of the analytical results of the expected output motion curve was 25.17%. The error of the analytical results of the expected output motion curve was 7.88%. The maximum thinning ratio of the analytical results of the prediction curve was 23.75%. The maximum error of the analytical results of the prediction curve was 6.47%, a decrease of 1.41%. The analytical results of the bottom dead center coining curve are demonstrated in Fig. 22b. The figure demonstrates that the trends of the experiment and analyzed thinning ratios were consistent. The maximum thinning ratio of the experiment was 19.17%, and the maximum thinning ratio of the analytical results of the expected output motion curve was 25.67%. The error of the analytical results of the expected output motion curve was 6.50%. The maximum thinning ratio of the analytical results of the prediction curve was 23.67%. The maximum error of the analytical results of the prediction curve was 4.50%, a decrease of 2.00%.

The analytical results of the pulsating curve with a pulse step of 1 mm are demonstrated in Fig. 22c. The figure reveals that the trend of the experiment and analyzed thinning ratio were consistent. The maximum thinning ratio of the experiment was 31.06%, and the maximum thinning ratio of the analytical results of the expected output motion curve was 37.25%. The error of the analytical results of the expected output motion curve was 6.19%. The maximum thinning ratio of the analytical results of the prediction curve was 33.25%. The maximum error of the analytical results of the prediction curve was 2.19%, a decrease of 4.00%. The analytical results of the pulsating curve with a pulse step of 3 mm are demonstrated in Fig. 22d. The figure demonstrated that the trend of the experiment and the analyzed thinning ratio were consistent. The maximum thinning ratio of the experiment was 29.34%, whereas the maximum thinning ratio of the analytical results of the expected output motion curve was 38.25%. The error of the analytical results of the expected output motion curve was 8.91%. The maximum thinning ratio of the analytical results of the prediction curve

Fig. 18 Different motion curves: (a) stepping curve, (b) bottom dead center coining curve, (c) pulsating curve with a pulse step of 1 mm, (d) pulsating curve with a pulse step of 3 mm, and (e) pulsating curve with a pulse step of 5 mm

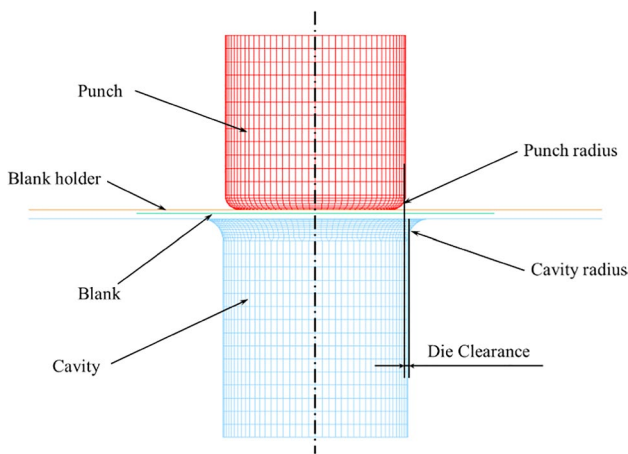
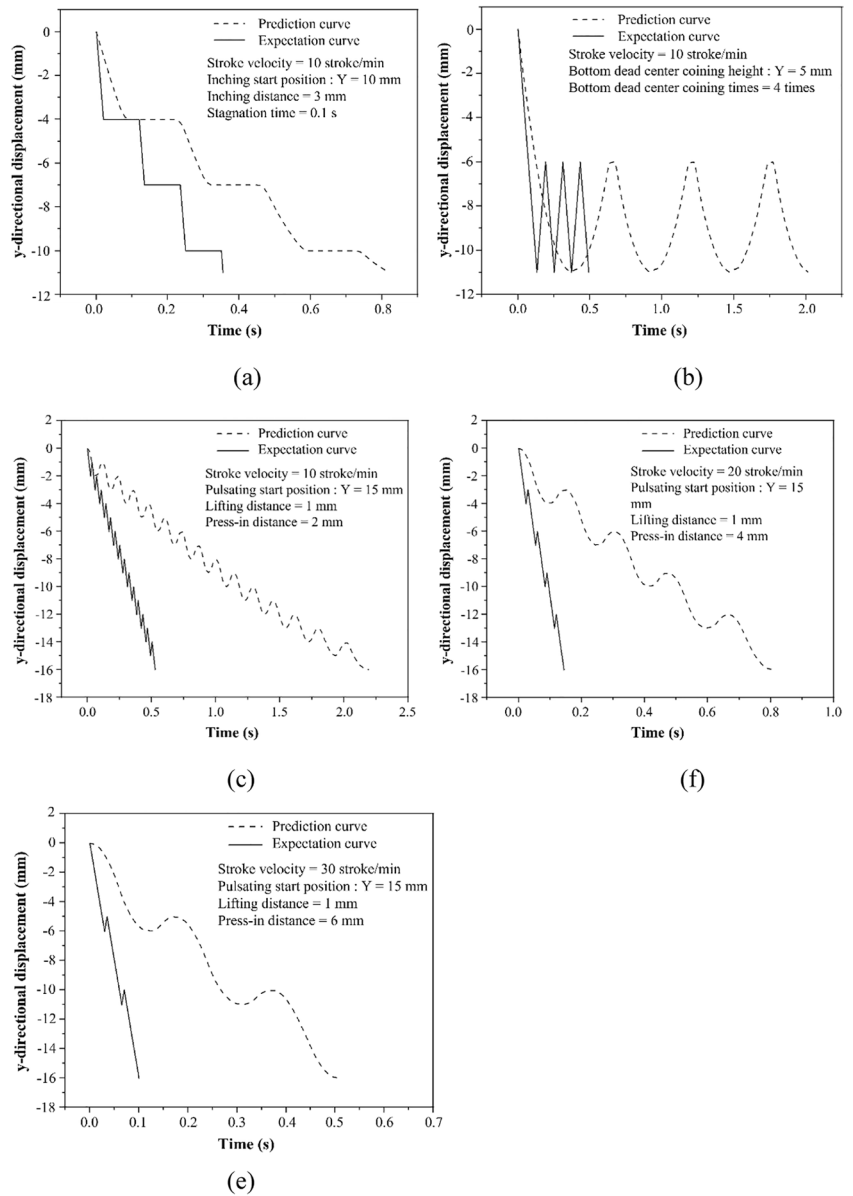


Fig. 19 DYNIFORM analysis model

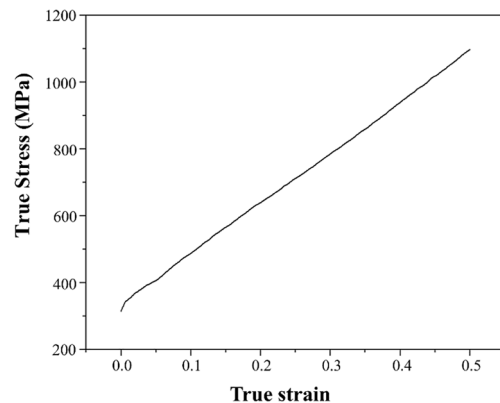


Fig. 20 SUS304 true stress–strain curve

Table 5 Material parameters of SUS304

Material property	Value
Blank thickness (mm)	1.2
Density (kg/mm ³)	7.83×10 ⁻⁶
Young's modulus (GPa)	207
Poisson's ratio	0.28
Yield strength (MPa)	239
Hardening index	0.193
Average plastic strain ratio	0.855

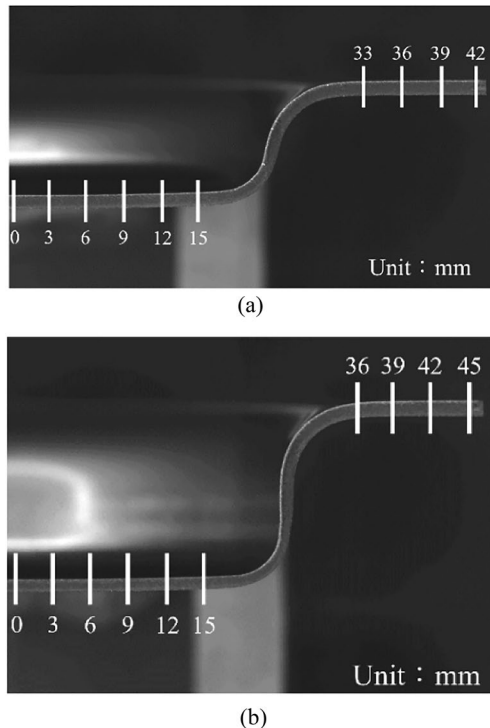


Fig. 21 **a** The measured positions of the stepping curve and coining curve and **(b)** the measured positions of the pulsating curves with a pulse step of 1, 3, and 5 mm

was 35.33%. The maximum error of the analytical results of the prediction curve was 5.99%, and the error decreased by 2.92%. The analytical results of the pulsating curve with a pulse step of 5 mm are illustrated in Fig. 22e. The figure reveals that the trends of the experiment and analyzed thinning ratios were consistent. The maximum thinning ratio of the experiment was 32.68%, whereas the maximum thinning ratio of the analytical results of the expected output motion curve was 39.00%. The error of the analytical results of the expected output motion curve was 6.32%. The maximum thinning ratio of the analytical results of the prediction curve was 36.92%. The maximum error of the analytical results of the prediction curve was 4.24%, a decrease of 2.08%. The thinning ratio analysis above shows that errors between the

analysis results of the predicted servo motion curve and the actual experiment are only 2~6%. Compared to the 6~9% error, the analysis result's accuracy improves. (However, the introduction of 2~6% error may be caused by stainless steel's high sensitivity behavior to strain rate and the coefficient of friction.)

(b) Verification of the forming force

The sensor equipment within the machine was used to obtain the forming force of the experiment, and the forming force of the experiment was compared with the analytical results of the prediction curve and the expected output motion curve. The results of the servo stepping curve are demonstrated in Fig. 23a. The maximum forming forces of the experiment, the expected output motion curve, and the prediction curve were 110,000 N, 118,191 N, and 113,672 N, respectively. The error of the analytical results of the expected output motion curve was 7.45%, and the error of the analytical results of the prediction curve was 3.34%, a decrease of 4.11%. The results of the bottom dead center coining curve are demonstrated in Fig. 23b. The maximum forming forces of the experiment, the expected output motion curve, and the prediction curve were 110,000 N, 117,080 N, and 114,913 N, respectively. The error of the analytical results of the expected output motion curve was 6.44%, and the error of the analytical results of the prediction curve was 4.90%, a decrease of 1.53%.

The results of the pulsating curve with a pulse step of 1 mm are illustrated in Fig. 23c. The maximum forming forces of the experiment, the expected output motion curve, and the prediction curve were 140,000 N, 144,960 N, and 139,450 N, respectively. The error of the analytical results of the expected output motion curve was 3.54%, and the error of the analytical results of the prediction curve was 0.09%, a decrease of 3.45%. The results of the pulsating curve with a pulse step of 3 mm are demonstrated in Fig. 23d. The maximum forming forces of the experiment, the expected output motion curve, and the prediction curve were 140,000 N, 146,699 N, and 143,974 N, respectively. The error of the analytical results of the expected output motion curve was 4.79%, and the error of the analytical results of the prediction curve was 2.84%, a decrease of 1.95%.

The results of the pulsating curve with a pulse step of 5 mm are illustrated in Fig. 23e. The maximum forming forces of the experiment, the expected output motion curve, and the prediction curve were 140,000 N, 146,424 N, and 143,635 N, respectively. The error of the analytical results of the expected output motion curve was 4.59%, and the error of the analytical results of the prediction curve was 2.6%, a decrease of 1.99%. Unlike the analytical values, the forming force of the experiment did not fluctuate greatly. This phenomenon was caused by the low

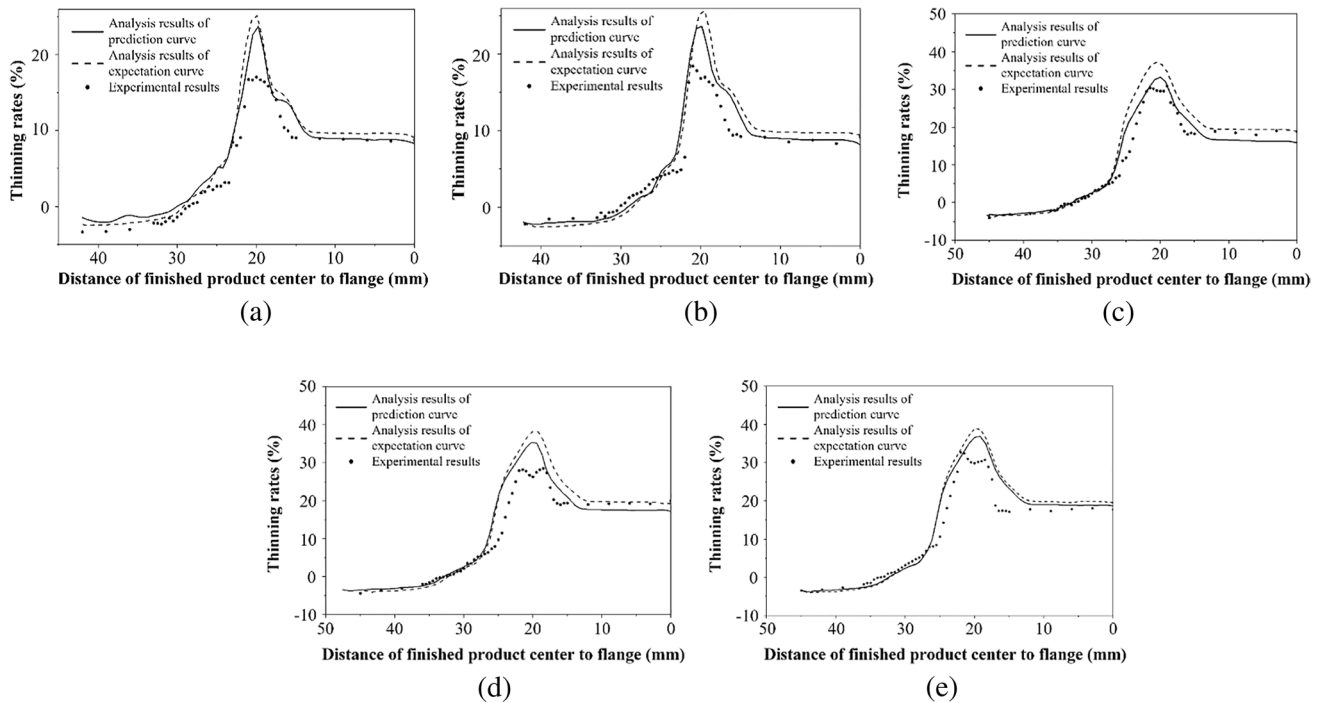


Fig. 22 Comparison of the thinning ratios between the analytical value and the experimental value: (a) stepping curve, (b) coining curve, (c) pulsating curve with a pulse step of 1 mm, (d) pulsating curve with a pulse step of 3 mm, and (e) pulsating curve with a pulse step of 5 mm

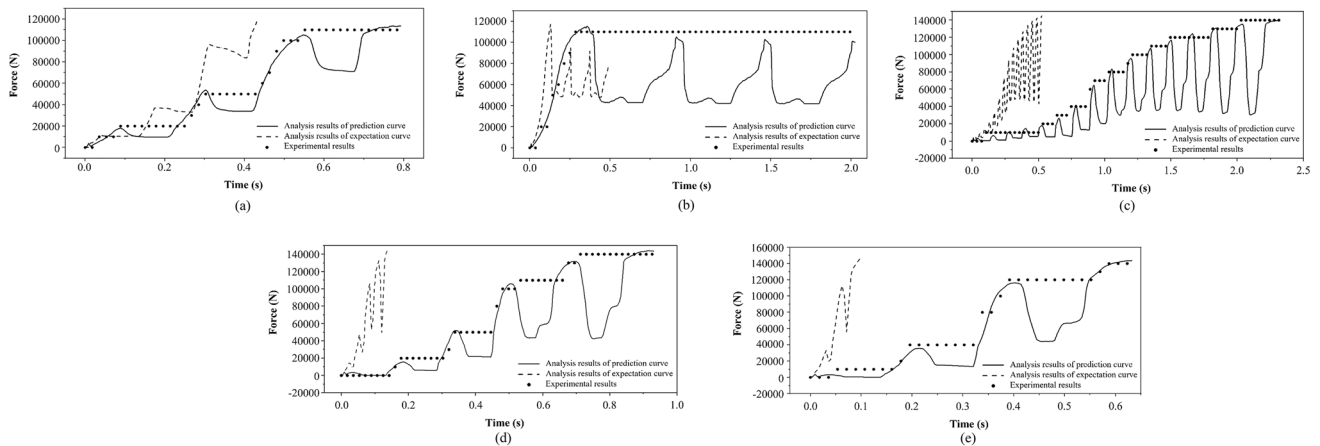


Fig. 23 Comparison between the analytical values and experimental values of the forming force: (a) stepping curve, (b) coining curve, (c) pulsating curve with a pulse step of 1 mm, (d) pulsating curve with a pulse step of 3 mm, and (e) pulsating curve with a pulse step of 5 mm

resolution of the sensor equipment of the machine and the low extraction velocity. According to the forming force result above, the analysis result using the predicted servo motion curve is close to the experimental results. Also, the position of forming force's peaks and valleys match with experimental results. Therefore, the results can be applied to product quality and deformation by structural deformation behavior when the stamping press and die are under load.

6 Conclusions

This study investigated and predicted the pulse motion curves of servo presses. The investigation was divided into two stages. The first stage analyzed the motion behavior of a direct-drive servo press and used MATLAB software to construct a theoretical model of the motion behavior of the direct-drive servo press to predict the motion curve.

The second stage aimed to reduce the time error of the prediction program of the motion curve. This study constructed a pulse trend surface database to optimize the prediction program. The experimental results demonstrated the following:

- (1) A large time error existed between the expected output motion curve and the true motion curve; the percentage error was 61.85%. This large time error occurred because the calculation of the expected output motion curve considered only the motion when the designated parameters were used and physical characteristics were ignored. Therefore, the assigned stroke velocity was used for both the initiation of the motion behavior and the change of the rotation direction of the servomotor.
- (2) The percentage error of the prediction curve before optimization was 13.84%. The error was 48.01% lower than that of the expected output motion curve. The error occurred because the prediction program considered only the linkage mechanism and acceleration and deceleration motion of the servo press during its calculations and ignored other factors such as the physical inertia of the machine, signal delay, and the loss of kinetic energy due to friction. Consequently, the second stage of this study established the database of the pulsating curve to optimize the prediction program and reduce the time error of the prediction.
- (3) The analytical results of the servo inching curve demonstrated that using the prediction curve instead of the expected output motion curve reduced the thinning ratio error from 7.88% to 6.47%, a decrease of 1.41%. In addition, using the prediction curve instead of the expected output motion curve reduced the forming force error from 7.45 to 3.34%, a decrease of 4.11%. The analytical results of the bottom dead center coining curve demonstrated that using the prediction curve instead of the expected output motion curve reduced the thinning ratio error from 6.50 to 4.50%, a decrease of 2.00%. In addition, using the prediction curve instead of the expected output motion curve reduced the forming force error from 6.44 to 4.90%, a decrease of 1.53%.
- (4) The analytical results of the pulsating curve with a pulse step of 1 mm demonstrated that using the prediction curve instead of the expected output motion curve reduced the thinning ratio error from 6.19% to 2.19%, a decrease of 4.00%. In addition, using the prediction curve instead of the expected output motion curve reduced the forming force error from 3.54% to 0.09%, a decrease of 3.45%. The analytical results of the pulsating curve with a pulse step of 3 mm demonstrated that using the prediction curve instead of the expected output motion curve reduced the thinning ratio error

from 8.91% to 5.99%, a decrease of 2.92%. In addition, using the prediction curve instead of the expected output motion curve reduced the forming force error from 4.79 to 2.84%, a decrease of 1.95%. The analytical results of the pulsating curve with a pulse step of 5 mm demonstrated that using the prediction curve instead of the expected output motion curve reduced the thinning ratio error from 6.32% to 4.24%, a decrease of 2.08%. In addition, using the prediction curve instead of the expected output motion curve reduced the forming force error from 4.59 to 2.60%, a decrease of 1.99%.

Author contribution The authors' contributions are as follows: all authors conceived and designed the study; Bor-Tsuen Lin, Chun-Chih Kuo, Kuo-Wang Liu, and Po-Hsien Li performed the theoretical deduction, performed the experiments and the finite element simulations, and performed the process optimization and analysis; Kuo-Wang Liu and Tse-Chang Li contributed to the interpretation of the results; Kuo-Wang Liu and Po-Hsien Li took the lead in writing the manuscript; Bor-Tsuen Lin, Tse-Chang Li and Chun-Chih Kuo contributed actively in writing the manuscript; all authors provided critical feedback and helped shape the research, analysis and manuscript.

Funding This study was financially supported by Taiwan's National Science and Technology Council (108–2221-E-992–064-MY3 and 111–2218-E-992–002) and the Frontier Metal Forming Research and Development Center from The Featured Areas Research Center Program within the framework of the Higher Education Sprout Project of Taiwan's Ministry of Education.

Data availability The datasets generated during and/or analyzed during the current study are available from the corresponding author on reasonable request.

Code availability Not applicable.

Declarations

Ethical approval The authors claim that none of the contents in this manuscript has been published or considered for publication elsewhere. Besides, the research contents of the article do not violate ethics.

Consent to participate This manuscript does not involve human or animal participation or data, therefore consent to participate is not applicable.

Consent to publish This manuscript does not contain data from any individual person; therefore, consent to publish is not applicable.

Competing interests The authors declare no competing interests.

References

1. Osakada K, Mori K, Altan T, Groche P (2011) Mechanical servo press technology for metal forming. *CIRP Ann Manuf Technol* 60:651–672

2. Matsumoto R, Jeon JY, Utsunomiya H (2013) Shape accuracy in the forming of deep holes with retreat and advance pulse ram motion on a servo press. *J Mater Process Technol* 213:770–778
3. Ju L, Patil S, Dykeman J, Altan T (2015) Forming of Al 5182-O in a servo press at room and elevated temperatures. *J Manuf Sci Eng* 137:051009
4. Groche P, Hoppe F, Sinz J (2017) Stiffness of multipoint servo presses: mechanics vs. control. *CIRP Ann Manuf Technol* 66:373–376
5. Song Y, Dai D, Geng P, Hua L (2017) Formability of aluminum alloy thin-walled cylinder parts by servo hot stamping. *Procedia Eng* 207:741–746
6. Olaizola J, Bouganis CS, de Argandona ES, Iturrospe A, Abete JM (2020) Real-time servo press force estimation based on dual particle filter. *IEEE Trans Ind Electron* 67:4088–4097
7. Hu G, Pan C (2020) Investigation of the plastic hardening of metal thin-walled tube under pulsating hydraulic loading condition. *J Mech Sci Technol* 34:4743–4751
8. Singh SK, Mahesh K, Kumar A, Swathi M (2020) Understanding formability of extra-deep drawing steel at elevated temperature using finite element simulation. *Mater Des* 31:4478–4484
9. Tommerup S, Endelt B (2012) Experimental verification of a deep drawing tool system for adaptive blank holder pressure distribution. *J Mater Process Technol* 212:2529–2540
10. Abe Y, Ohmi T, Mori K, Masuda T (2014) Improvement of formability in deep drawing of ultra-high strength steel sheets by coating of die. *J Mater Process Technol* 214:1838–1843
11. Cui X, Li J, Mo J, Fang J, Zhou B, Xiao X (2016) Incremental electromagnetic-assisted stamping (IEMAS) with radial magnetic pressure: a novel deep drawing method for forming aluminum alloy sheets. *J Mater Process Technol* 233:79–88
12. Zheng K, Lee J, Lin J, Dean TA (2017) A buckling model for flange wrinkling in hot deep drawing aluminium alloys with macro-textured tool surfaces. *Int J Mach Tools Manuf* 114:21–34
13. Cao Q, Du L, Li Z, Lai Z, Li Z, Chen M, Li X, Xu S, Chen Q, Han X, Li L (2019) Investigation of the Lorentz-force-driven sheet metal stamping process for cylindrical cup forming. *J Mater Process Technol* 271:532–541
14. Ha J, Breunig A, Fones J, Hoppe F, Korkolis YP, Groche P, Kinsey BL (2019) AA1100-O cylindrical cup-drawing using 3D servo-press. *IOP Conf Ser Mater Sci Eng* 651:012094
15. Chen K, Korkolis YP (2020) Industry 4.0 in stamping: a wrinkling indicator for reduced-order modeling of deep-drawing processes. *Procedia Manuf* 51:864–869
16. Manoochehri M, Kolahan F (2014) Integration of artificial neural network and simulated annealing algorithm to optimize deep drawing process. *Int J Adv Manuf Technol* 73:241–249
17. Abe Y, Mori K, Maeno T, Ishihara S, Kato Y (2019) Improvement of sheet metal formability by local work-hardening with punch indentation. *Prod Eng Res Devel* 13:589–597
18. Si S, Wu Q, Mei D, Mao W, Song S, Xu L, Zuo T, Wang Y (2022) Numerical simulation and experiment of microstamping process to fabricate multi-channel of SUS304 thin sheets with different grain size. *Int J Adv Manuf Technol* 121:6739–6750
19. Cios G, Tokarski T, Żywczak A, Dziurka R, Stępień M, Gondek Ł, Marciszko M, Pawłowski B, Wiczerczak K, Bała P (2017) The investigation of strain-induced martensite reverse transformation in AISI 304 austenitic stainless steel. *Metall Mater Trans A* 48:4999–5008
20. Acharya S, Moitra A, Bysakh S, Nanibabu M, Krishanan SA, Mukhopadhyay CK, Rajkumar KV, Sasikala G, Mukhopadhyay A, Mondal DK, Ghosh KS, Jha BB, Muraleedharana K (2019) Effect of high strain rate deformation on the properties of SS304L and SS316LN alloys. *Mech Mater* 136:103073
21. Sunil S, Kapoor R (2020) Effect of strain rate on the formation of strain-induced martensite in AISI 304L stainless steel. *Metall Mater Trans A* 51:5667–5676
22. Li T, Kuo C, Yang C, Liu K, Li P, Lin B (2022) Influence of motion curve errors of direct-drive servo press on stamping properties. *Int J Adv Manuf Technol* 120:4461–4476
23. Tso PL (2010) Optimal design of a hybrid-driven servo press and experimental verification. *J Mech Design* 132:034503
24. He J, Gao F, Bai Y (2013) A two-step calibration methodology of multi-actuated mechanical servo press with parallel topology. *Meas* 46:2269–2277
25. Song Q, Guo B, Li J (2013) Drawing motion profile planning and optimizing for heavy servo press. *Int J Adv Manuf Technol* 69:2819–2831
26. Kim SY, Tsuruoka K, Yamamoto T (2014) Effect of forming speed in precision forging process evaluated using CAE technology and high performance servo-press machine. *Procedia Eng* 81:2415–2420
27. Kütük ME, Dülger LC (2016) A hybrid press system: Motion design and inverse kinematics issues. *Eng Sci Technol an Int J* 19:846–856
28. Sencer B, Tajima S (2017) Frequency optimal feed motion planning in computer numerical controlled machine tools for vibration avoidance. *J Manuf Sci Eng* 139:011006
29. Halicioğlu R, Dulger LC, Bozdana AT (2018) Improvement of metal forming quality by motion design. *Robot Comput Integr Manuf* 51:112–120
30. Li C, Tso P (2008) Experimental study on a hybrid-driven servo press using iterative learning control. *Int J Mach Tools Manuf* 48:209–219
31. Halicioğlu R, Dulger LC, Bozdana AT (2017) Modeling, design, and implementation of a servo press for metal-forming application. *Int J Adv Manuf Technol* 91:2689–2700
32. Chen T, Chen S, Wang C (2022) Punch motion curve in the extrusion–drawing process to obtain circular cups. *Machines* 10:638

Publisher's note Springer Nature remains neutral with regard to jurisdictional claims in published maps and institutional affiliations.

Springer Nature or its licensor (e.g. a society or other partner) holds exclusive rights to this article under a publishing agreement with the author(s) or other rightsholder(s); author self-archiving of the accepted manuscript version of this article is solely governed by the terms of such publishing agreement and applicable law.